

Three-dimensional particle image velocimetry: experimental error analysis of a digital angular stereoscopic system

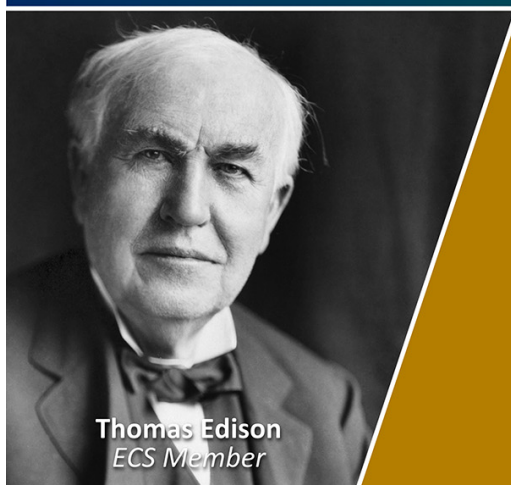
To cite this article: N J Lawson and J Wu 1997 *Meas. Sci. Technol.* **8** 1455

You may also like

- [Direct comparison of 2D PIV and stereoscopic PIV measurements](#)
Jong-Hwan Yoon and Sang-Joon Lee
- [Editorial](#)
M Trinité and B Lecordier
- [Standard images for particle-image velocimetry](#)
K Okamoto, S Nishio, T Saga et al.

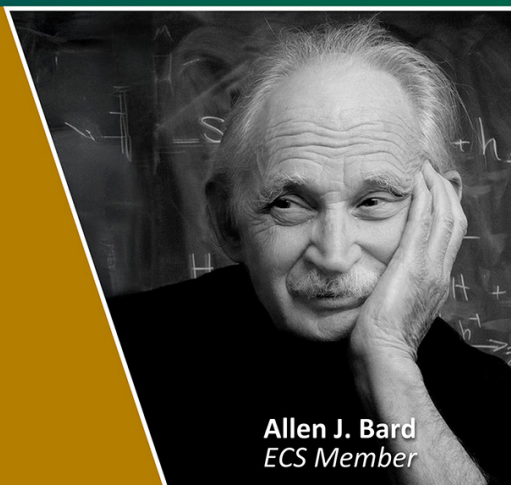
View the [article online](#) for updates and enhancements.

Join the Society
Led by Scientists,
for *Scientists Like You!*



The
Electrochemical
Society

Advancing solid state &
electrochemical science & technology



Three-dimensional particle image velocimetry: experimental error analysis of a digital angular stereoscopic system

N J Lawson[†] and J Wu[‡]

[†] The GK Williams CRC, Department of Chemical Engineering,
The University of Melbourne, Parkville, Victoria 3052, Australia

[‡] CSIRO, Division of Building, Construction and Engineering, Graham Road,
Highett, Victoria 3190, Australia

Received 22 July 1997, accepted for publication 25 September 1997

Abstract. Experimental error analysis of a digital angular stereoscopic PIV system is presented. The paper firstly describes an experimental rig which includes the design of a novel PIV test block for *in situ* calibration. This allowed the user to set up a static seeded flow volume which was translated in and out of plane to record PIV images using two megapixel CCD cameras positioned for angular stereoscopic viewing. PIV data were collected for a range of camera angles up to 45° and for a range of flow displacements and processed by cross correlation into a set of two-dimensional calibration and flow displacement vectors. These 2D data were then processed into three-dimensional data by the use of geometric and bicubic spline interpolation algorithms and an error analysis performed on the predicted displacements. Results from this analysis have shown optimum system performance will be obtained by using camera angles of between 20 and 30° and *f* numbers of *f*16 and higher. The results have also shown a theoretical prediction of system performance derived in previous work, which considers the ratio of out of plane to in plane errors, matches to within 8 and 18% of the experimental system performance.

1. Introduction

The measurement of fluid flows in engineering has continually generated innovative techniques varying from a simple Pitot tube [1] to complex laser techniques [2]. Particle image velocimetry (PIV) is a recent but well established, non-intrusive technique for the measurement of mean and instantaneous fluid velocity from a single plane of interest [3,4]. PIV in its simplest form involves placing a pulsed laser sheet into the measured fluid flow plane and recording the position of seeding particles by the use of double-exposure photography. This results in a transparency consisting of a large number of particle image pairs whose average displacement over each small region of the photograph is a measure of the mean velocity at the corresponding point in the fluid. From the developed transparency, a two-dimensional (2D) velocity map is then extracted by using optical or digital spatial correlation analysis to determine the particle displacement within each small region of the flow [5,6].

The application of PIV to increasingly complex fluid flows [7,8] has resulted in the demand for three-dimensional (3D) measurements and the development

of 3D PIV techniques. A recent review of 3D PIV highlighted the different methods that had been successfully demonstrated at that time [9]. These were mainly holographic PIV (HPIV) [10,11] and stereoscopic PIV methods [12–16]. More recent methods have included dual-plane PIV [17,18] and off axis stereoscopic PIV [19]. If these techniques are considered in terms of their imaging and data processing systems, HPIV is the most demanding in both cases requiring complex optics and advanced data processing techniques. In contrast dual-plane PIV and stereoscopic PIV only require conventional cameras and light sheet arrangements although intensive image processing is necessary.

Any PIV system will have a level of accuracy which will determine the validity of its application. Previous authors have investigated in detail the error characteristics of a simple 2D PIV system [20–22]. To date, however, limited work has been carried out on the error characteristics of 3D PIV systems and has mainly been restricted to stereoscopic configurations [12,13,19]. This previous work has recently been extended by the present authors to give a set of theoretical design curves for stereoscopic systems [23]. These characteristics allowed

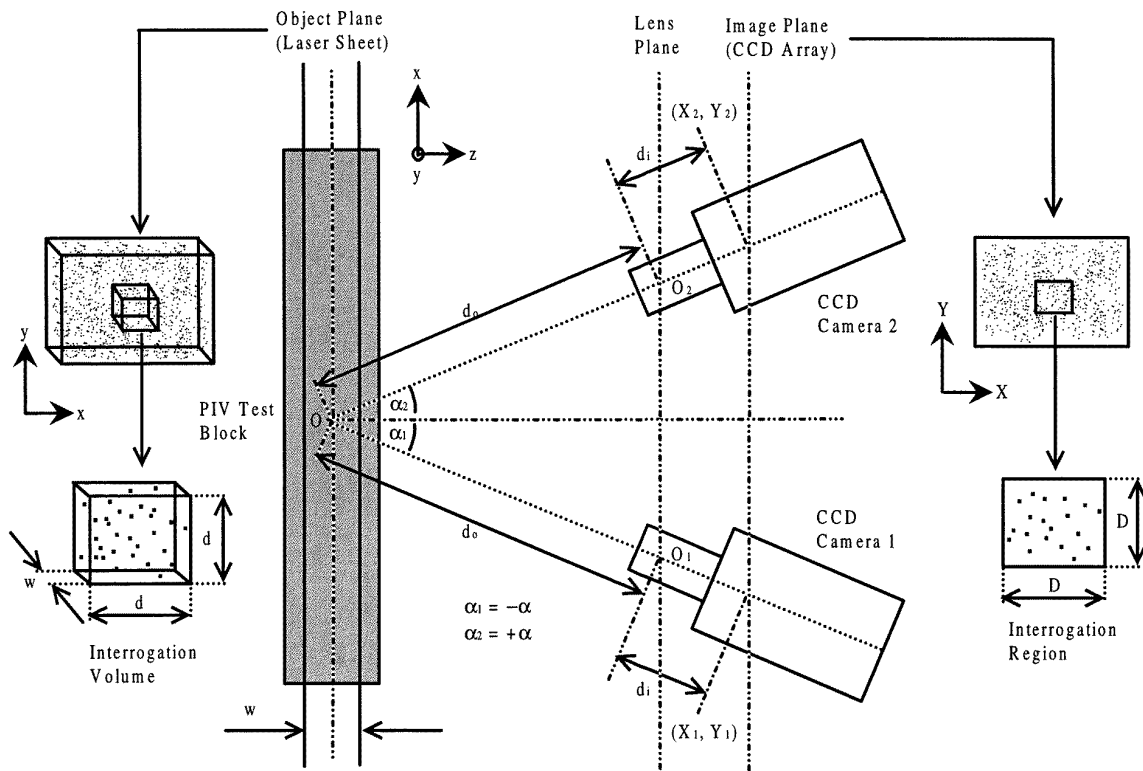


Figure 1. Diagram of experimental stereoscopic imaging system.

the overall performance of an angular or translational stereoscopic system to be analysed for a range of camera angles and separations.

In what follows, experimental work is presented which aims to validate the theory outlined in the previous work [23]. The analysis is based on a digital angular stereoscopic system which is used to investigate the system performance over a range of camera angles and fluid displacements. These experimental results are then directly compared to the theoretical predictions and any discrepancies discussed.

2. Experimental technique

The following section describes the stereoscopic imaging system and data acquisition methods used to obtain the experimental PIV data. The system was based on a direct calibration method by using a design of a PIV test block developed for the project. This method assumed acceptable linearity between the object and image planes by using an appropriate object distance and resulted in a much simplified image processing routine which could use conventional correlation and interpolation routines for the calculations. This section also describes the testing procedures adopted and analysis of the error ratio characteristics from experimental error data.

2.1. Imaging system

Figure 1 illustrates the stereoscopic imaging system used to record the PIV data. In the imaging plane two Kodak

MegaPlus CCD cameras were mounted onto separate rotation stages at an angle α to the z axis where $\alpha_1 = -\alpha$ and $\alpha_2 = +\alpha$. These stages were then both mounted onto two x translation platforms which were secured onto one end of an optical breadboard at an appropriate separation. This system allowed fine adjustment of the camera positions to achieve camera angles up to 45° , camera separations in x up to 600 mm and object distances up to 800 mm. Resolution of the translation stages was $10 \mu\text{m}$ and the rotation stages $1/10$ of a degree. Both cameras had a resolution of 1280×1024 pixels with 8-bit greyscale output and an array size of $10 \text{ mm} \times 8 \text{ mm}$. All the PIV images were recorded using 60 mm Nikon Micro-Nikor lenses. A lens f number of $f16$ was used for camera angles up to $\alpha = 30^\circ$ and $f22$ for any camera angles above this. These f numbers were based on recommendations for depth of field by Adrian [3].

The object plane consisted of an x - z translation stage centred about the origin O as shown in figure 1 and a light sheet system connected to a 4 W argon ion light source through a fibre-optic delivery. On top of the translation stages a fixed bracket was used to mount the calibration grid or PIV test block and provided exact alignment with the laser sheet for each set of measurements. The light sheet system was coupled to the fibre optic through a mounting block which contained a collimation lens and glass rod. This allowed adjustment of the light sheet divergence and the light sheet thickness, w , which was eventually set to 2.5 mm for all imaging. The object distance, d_o , as defined in figure 1 was set to 380 mm for all camera angles. Both

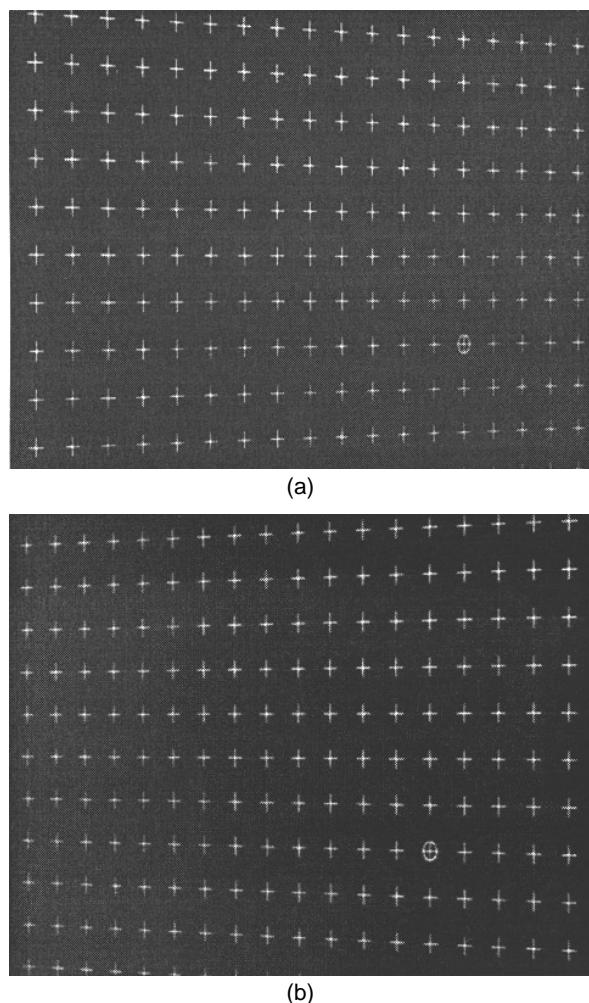


Figure 2. (a) Left-hand CCD image of calibration grid. (b) Right-hand CCD image of calibration grid ($\alpha = 45^\circ$).



Figure 3. Typical PIV image from PIV test block ($\alpha = 45^\circ$).

these constants ensured that equal displacements of the test block in the x and z axes would produce equal percentages of movement in terms of a percentage of the interrogation region length d , or a percentage of the light sheet width w at the origin O .

2.2. PIV test blocks

Previous PIV test methods have used glass plates coated with seeding and adhesive with conventional flood illumination for imaging [13,21]. In the following, however, an alternative test method is presented based on a design of PIV test block. This method allows a PIV light source to be used and provides realistic seeding characteristics such as those found in the measured fluid. The technique also allows the recording of a combination of in and out of plane data and can be adjusted to provide a wide range of particle image sizes and particle seeding densities if required. In addition the test blocks introduce imperfections such as background scatter and image aberrations that are normally present on PIV recordings but which are not normally present in computer simulated data.

The PIV test blocks consist of hollow glass spheres suspended in solid clear araldite blocks. The araldite blocks were manufactured by permanently setting Ciba Geigy Araldite resin M with hardener HY6150 into open-top glass containers. The glass containers, with internal dimensions $20 \text{ mm} \times 350 \text{ mm} \times 250 \text{ mm}$, were constructed from 2 mm thick sheet glass pieces adhered together with silicone sealant. This method gave acceptable viewing properties with good non-scratch characteristics. Air bubbles which formed in the resin during mixing with the hardener were removed by placing the mould in a 100 kPa vacuum for one hour before allowing the block to set.

The particles used to seed the test blocks were Potters Ballotini SphericeTM hollow glass spheres. They were chosen because of their excellent scattering properties in the resin. The original $45\text{--}100 \mu\text{m}$ diameter range was wire mesh sieved down to a $45\text{--}60 \mu\text{m}$ size range before seeding the resin so as to improve the homogeneity of the sample. Approximate seeding densities were determined by the amount of seeding weight added to the resin before moulding.

2.3. Calibration and data acquisition

A calibration stage is necessary for stereoscopic systems since the imaging geometry generally causes significant aberrations [12,13,16]. The calibration procedure will output a space and calibration coefficient map across the image where the calibration coefficients are related to the spatial distortion of the image. This distortion becomes significant when imaging inside a wide fluid layer and complex stereoscopic equations can be developed to output the calibration coefficients [12]. In this case, however, a simpler direct *in situ* calibration method was developed based on the PIV test blocks and which relied on acceptable linearity between the object and image plane by using an appropriate object distance. To this end an object distance of 380 mm was selected and linearity tested at the calibration stage for a range of PIV test block translations. This approach resulted in a basic image processing algorithm which used readily available correlation and interpolation routines.

For calibration a grid was placed in the centre of the light sheet or object plane. This grid allowed alignment of

the camera positions in the x plane with a grid origin so that both cameras were imaging a common object plane. Figures 2(a) and 2(b) illustrate the left and right calibration grid images which have 5 mm grid spacing in x and y and where the grid origin can clearly be seen. The grid images also allowed calibration of the x and y axis space coordinates by using the data processing software described in the next section. To obtain the calibration coefficients two exposures were recorded from the PIV test block with translations between exposures of 200–800 μm in the x or z axes. These displacements corresponded to 7.5–30% of the interrogation region length d at O or the light sheet width w . The y axis was not required for this analysis. Figure 3 illustrates a typical PIV image obtained from the test blocks. These data were subsequently processed into x and z calibration coefficients by cross correlation software described in the next section.

For test data acquisition a similar procedure was used as for the x and z calibration coefficients. In this case, however, in order to obtain suitable data for the error analysis, the block was translated by an equal amount in both the x and z axes. As before the translations chosen were between 200 and 800 μm in z and x axes which corresponded to a range of 7.5–30% of the interrogation region length d at O and the light sheet width w .

2.4. Data processing

Figure 4 illustrates the data processing procedure used to calculate the x , y and z components of particle displacement Δx , Δy and Δz . The procedure can be split into three major parts. Each part uses simple correlation and interpolation algorithms due to the assumption of linearity between the object and image planes and the decoupling of the x and z characteristics. Three data processing routines were developed to perform the calculations for each part. The first two involved calibration of the system and the third the calculation of the three-dimensional displacement components. The y axis was not required for the error analysis but the relevant equations will still be listed for completeness.

In the first routine calibration grid image data were initially processed into the X and Y pixel coordinate functions $X_1(x, y)$, $X_2(x, y)$ and $Y_1(x, y)$, $Y_2(x, y)$. These functions were produced by performing centroid analysis on the image across an $M_g \times N_g$ grid at points (X_1^i, Y_1^j) and (X_2^i, Y_2^j) where i and j are the gridpoint numbers. These centroid pixel positions were then fed into a bicubic spline interpolation routine ([24], pp 99–122). The actual positions of x and y in space were determined from the gridpoint data and spacing. A threshold was also used to eliminate background image noise with a value set from a histogram analysis of the images. The resulting bicubic spline interpolation functions were used in all subsequent image processing to reference any image pixel position X_1 , Y_1 and X_2 , Y_2 into an actual space position x and y and vice versa.

The second processing routine was used to produce the x , y and z calibration coefficient functions from the PIV calibration images. This was done by correlating the pairs

of images on a regularly spaced i, j image grid using the cross correlation functions

$$R_1(\xi, \eta)_{i,j} = \int_{-\infty}^{+\infty} \int_{-\infty}^{+\infty} G_1(X_1^{cc}, Y_1^{cc})_{i,j} \times H_1(X_1^{cc} - \xi, Y_1^{cc} - \eta)_{i,j} dX_1^{cc} dY_1^{cc} \quad (1)$$

and

$$R_2(\xi, \eta)_{i,j} = \int_{-\infty}^{+\infty} \int_{-\infty}^{+\infty} G_2(X_2^{cc}, Y_2^{cc})_{i,j} \times H_2(X_2^{cc} - \xi, Y_2^{cc} - \eta)_{i,j} dX_2^{cc} dY_2^{cc} \quad (2)$$

where $G_1(X_1^{cc}, Y_1^{cc})_{i,j}$, $G_2(X_2^{cc}, Y_2^{cc})_{i,j}$ and $H_1(X_1^{cc}, Y_1^{cc})_{i,j}$, $H_2(X_2^{cc}, Y_2^{cc})_{i,j}$ are the first- and second-exposure interrogation region images respectively and $R_1(\xi, \eta)_{i,j}$, $R_2(\xi, \eta)_{i,j}$ are the correlation outputs at gridpoint (i, j) [25]. The correlation routine was based on a fast Fourier transform (FFT) algorithm ([24], pp 530–602). A centroid routine was performed on the three highest peaks in the correlation plane and the peak positions stored for post-processing. The interrogation region resolution was set to 64×64 pixels with a 50% overlap and a 4×4 pixel centroid sample to provide sufficient accuracy [26]. The post-processing initially involved validating the vectors using a range set by visual inspection of the output vector maps. Finally the x and z calibration data were calculated by taking the correlation vector component, $R_1(\xi, 0)_{i,j}$ or $R_2(\xi, 0)_{i,j}$, and interpolating and smoothing to reduce correlation noise as recommended by previous workers [27]. For the y calibration the Y component vector was taken, $R_1(0, \eta)_{i,j}$ or $R_2(0, \eta)_{i,j}$, and interpolated and smoothed as before. To convert these data into the x , y and z calibration coefficient functions the correlation data were initially converted to a pixel mm^{-1} quantity at each grid point (X_1^i, Y_1^j) and (X_2^i, Y_2^j) such that:

$$a_1(X_1^i, Y_1^j) = \frac{R_1(\xi, 0)_{i,j}}{\Delta x_{cal}} \bigg|_{j=1, N_{cal}}^{i=1, M_{cal}} \quad (3)$$

$$a_2(X_2^i, Y_2^j) = \frac{R_2(\xi, 0)_{i,j}}{\Delta x_{cal}} \bigg|_{j=1, N_{cal}}^{i=1, M_{cal}} \quad (4)$$

$$b_1(X_1^i, Y_1^j) = \frac{R_1(0, \eta)_{i,j}}{\Delta z_{cal}} \bigg|_{j=1, N_{cal}}^{i=1, M_{cal}} \quad (5)$$

$$b_2(X_2^i, Y_2^j) = \frac{R_2(0, \eta)_{i,j}}{\Delta z_{cal}} \bigg|_{i,j}^{i=1, M_{cal}} \quad (6)$$

$$c_1(X_1^i, Y_1^j) = \frac{R_1(0, \eta)_{i,j}}{\Delta y_{cal}} \bigg|_{j=1, N_{cal}}^{i=1, M_{cal}} \quad (7)$$

$$c_2(X_2^i, Y_2^j) = \frac{R_2(0, \eta)_{i,j}}{\Delta y_{cal}} \bigg|_{i,j}^{i=1, M_{cal}} \quad (8)$$

where M_{cal} , N_{cal} is the grid size for the a, b and c coefficients and Δx_{cal} , Δy_{cal} and Δz_{cal} are the PIV test block calibration displacements in the x , y and z axes. These data were fed into a bicubic spline interpolation routine to produce the calibration coefficient functions $a_1(X_1, Y_1)$, $a_2(X_2, Y_2)$, $b_1(X_1, Y_1)$, $b_2(X_2, Y_2)$ and $c_1(X_1, Y_1)$, $c_2(X_2, Y_2)$ which allow estimates of the

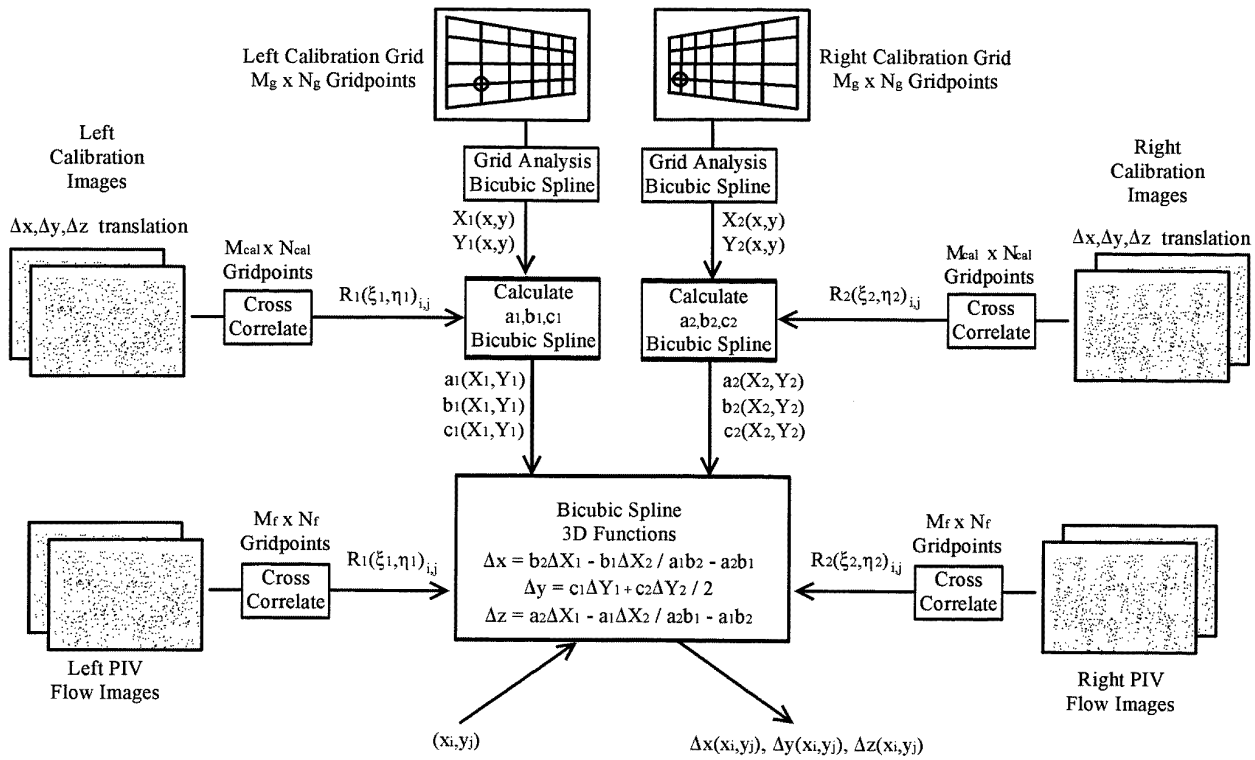


Figure 4. Illustration of data processing procedure used to calculate Δx , Δy and Δz particle displacements.

x , y and z calibration coefficients at any pixel position on the image. All the $a_1, a_2, b_1, b_2, c_1, c_2$ coefficients and X_1, X_2, Y_1, Y_2 interpolation functions were subsequently stored onto a batch file for use in the third and final data processing routine.

The third processing routine was used to calculate three-dimensional data from actual PIV flow data or in this case test data recorded from the PIV test blocks. In the first stage of the calculation, the two sets of left and right flow images were cross correlated, validated and smoothed using a regularly spaced i, j grid as described previously and stored into the displacement arrays, $\Delta X_1(X_1^i, Y_1^j)$, $\Delta Y_1(X_1^i, Y_1^j)$ and $\Delta X_2(X_2^i, Y_2^j)$, $\Delta Y_2(X_2^i, Y_2^j)$ where

$$\Delta X_1(X_1^i, Y_1^j) = R_1(\xi, 0)_{i,j}^{i=1, M_f, j=1, N_f} \quad (9)$$

$$\Delta Y_1(X_1^i, Y_1^j) = R_1(0, \eta)_{i,j}^{i=1, M_f, j=1, N_f} \quad (10)$$

$$\Delta X_2(X_2^i, Y_2^j) = R_2(\xi, 0)_{i,j}^{i=1, M_f, j=1, N_f} \quad (11)$$

$$\Delta Y_2(X_2^i, Y_2^j) = R_2(0, \eta)_{i,j}^{i=1, M_f, j=1, N_f} \quad (12)$$

and M_f, N_f are the flow grid sizes. These data were also fed into a bicubic spline interpolation to yield the displacement functions $\Delta X_1(X_1, Y_1)$, $\Delta Y_1(X_1, Y_1)$ and $\Delta X_2(X_2, Y_2)$, $\Delta Y_2(X_2, Y_2)$. These functions allowed an estimate of the particle image displacement in X or Y at any pixel position on the left and right images.

From these displacement functions and the calibration coefficient functions $a_1(X_1, Y_1)$, $a_2(X_2, Y_2)$, $b_1(X_1, Y_1)$, $b_2(X_2, Y_2)$ and $c_1(X_1, Y_1)$, $c_2(X_2, Y_2)$ an estimate of the three components of particle displacement, ($\Delta x, \Delta y, \Delta z$), can be made at any point (x_i, y_j) inside the calibrated flow area using previous simple gas interface stereoscopic derivations as follows [12, 23, 26]:

$$\Delta x(x_i, y_j) = \frac{b_2(X_2^i, Y_2^j) \Delta X_1(X_1^i, Y_1^j) - b_1(X_1^i, Y_1^j) \Delta X_2(X_2^i, Y_2^j)}{a_1(X_1^i, Y_1^j) b_2(X_2^i, Y_2^j) - a_2(X_2^i, Y_2^j) b_1(X_1^i, Y_1^j)} \quad (13)$$

$$\Delta y(x_i, y_j) = \frac{c_1(X_1^i, Y_1^j) \Delta Y_1(X_1^i, Y_1^j) + c_2(X_2^i, Y_2^j) \Delta Y_2(X_2^i, Y_2^j)}{2} \quad (14)$$

$$\Delta z(x_i, y_j) = \frac{a_2(X_2^i, Y_2^j) \Delta X_1(X_1^i, Y_1^j) - a_1(X_1^i, Y_1^j) \Delta X_2(X_2^i, Y_2^j)}{a_2(X_2^i, Y_2^j) b_1(X_1^i, Y_1^j) - a_1(X_1^i, Y_1^j) b_2(X_2^i, Y_2^j)} \quad (15)$$

where the image coordinates (X_1^i, Y_1^j) and (X_2^i, Y_2^j) are found from the X, Y coordinate functions:

$$X_1^i = X_1(x_i, y_i) \quad (16)$$

$$Y_1^j = Y_1(x_i, y_i) \quad (17)$$

$$X_2^i = X_2(x_i, y_i) \quad (18)$$

$$Y_2^j = Y_2(x_i, y_i). \quad (19)$$

2.5. Error analysis

In order to compare the experimental data with the theoretical error model [23], analysis was carried out on the output displacement data Δx and Δz . This consisted of examining the rms errors $\delta_{rms}(\Delta x)$ and $\delta_{rms}(\Delta z)$ in Δx and Δz across a regular i, j flow grid with M by N gridpoints such that:

$$\delta_{rms}(\Delta x) = \frac{1}{MN \Delta x_{cal}} \sqrt{\sum_{i=1, j=1}^{M, N} [\Delta x_{cal} - \Delta x(x_i, y_j)]^2} \quad (20)$$

$$\delta_{rms}(\Delta z) = \frac{1}{MN \Delta z_{cal}} \sqrt{\sum_{i=1, j=1}^{M, N} [\Delta z_{cal} - \Delta z(x_i, y_j)]^2}. \quad (21)$$

Errors outside two standard deviations of the data $[\Delta x_{cal} - \Delta x(x_i, y_j)]$ and $[\Delta z_{cal} - \Delta z(x_i, y_j)]$ were rejected to filter out spurious measurements and 4000 gridpoints were used for the analysis. To compare the results to previous theoretical analysis [23], the experimental error ratio, e_r , was found from:

$$e_r = \frac{\delta_{rms}(\Delta z)}{\delta_{rms}(\Delta x)}. \quad (22)$$

The next section will now show the results from the error analysis for a range of camera angles and fluid displacements.

3. Results

Considering the assumption of linearity, we must first examine this characteristic for a range of camera angles and test block translations. Figure 5 shows the a and b calibration coefficients obtained at $x/d_0 = 0.1$ or the edge of the image where maximum distortion will occur. In each case two sets of test block translations were made from 200 to 800 μm in the x axes and z axes. These results show, for camera angles of $\alpha = 15^\circ$ and $\alpha = 30^\circ$, that the system clearly behaves with acceptable linearity in both axes.

If we now examine the individual displacement errors in x and z it can be seen from figure 6 that significant errors in the z component begin to occur as the camera angle is decreased from $\alpha = 45^\circ$ to $\alpha = 10^\circ$. For example the rms error in z at $\alpha = 45^\circ$ is 4% rising to a maximum of 13% at $\alpha = 10^\circ$. In contrast the x component error slowly increases with camera angle from around 1% at $\alpha = 10^\circ$ to 3–4% at $\alpha = 45^\circ$. These counteracting effects are caused by the geometric and imaging properties of the system. In z the error will mainly be dependent on camera geometry since an increase in camera angle will result in greater imaging sensitivity to a z displacement and hence a lower measurement error. In x , however, greater camera angles will cause increased imaging problems such as aberrations with a resultant increase in the x error. Therefore a compromise must be sought between acceptable imaging quality and the required z accuracy and these initial results suggest the optimum range of camera angle to be $20^\circ < \alpha < 30^\circ$.

The results in figure 6 also show a dependence on particle displacement with a greater displacement giving improved accuracy. These effects can be attributed to the noise characteristics of the correlation function which has a random error primarily dependent on particle image size, seeding density and velocity gradient [20, 22]. Therefore because the noise is generally independent of particle image displacement, a smaller particle displacement will result in a greater rms % error as shown in the results.

If we now examine the error ratio characteristics for the system, shown in figure 7, it can be seen that the experimental trends match the theoretical predictions well. The theoretical trend follows a $1/\tan \alpha$ function [23]. These theoretical errors are illustrated more clearly in figure 8 which shows the percentage errors in the prediction compared with the experimental results for a range of camera angles and particle displacements. It can be seen that the discrepancies in the predictions are worst at the smallest particle displacement of 7.5% of d and w with a overall error of 38%. This error, however, falls to around 8 and 18% at the larger particle displacements of 15 and 30% of d and w . This improvement is again related to the noise characteristics of the correlation function and the resultant fall in rms error with increasing particle image displacement. The poorer performance with smaller displacements is also apparent if the error characteristics in x are examined. These are shown in figure 9 for a range of $-0.1 < x/d_0 < 0.1$ and the deviation of the experimental results from the theoretical prediction clearly becomes worst at the lower particle displacements.

These results have suggested an optimum range of camera angle of $20^\circ < \alpha < 30^\circ$ and also have shown the theoretical predictions give an acceptable approximation to the actual performance of the angular system. The next section will now discuss these results and their application in more detail.

4. Discussion

The angular stereo system tested has successfully shown error ratios of $e_r < 2$ can be achieved by using a relatively simple CCD camera set-up providing the camera angle is greater than 30° and providing an f number of $f/16$ or higher is used. This performance, however, does degrade as the particle displacement being measured is reduced. This limitation could be improved by using a higher-resolution CCD or a 5 in \times 4 in photographic camera format as demonstrated by previous workers [12, 13]. This would allow the interrogation region resolution to be increased which will produce in a fall in the x rms error. An additional benefit in the increase in image resolution is a corresponding increase in spatial resolution which must be matched to the flow structures being measured [3]. The use of a high-resolution photographic system would also allow the user to use a more sophisticated angular configuration such as the Scheimpflug system proposed by previous workers [16]. In this case the camera back was tilted by an predetermined angle and a novel liquid prism used to reduce image aberrations at a given f number. This resulted in an equivalent image quality being achieved with

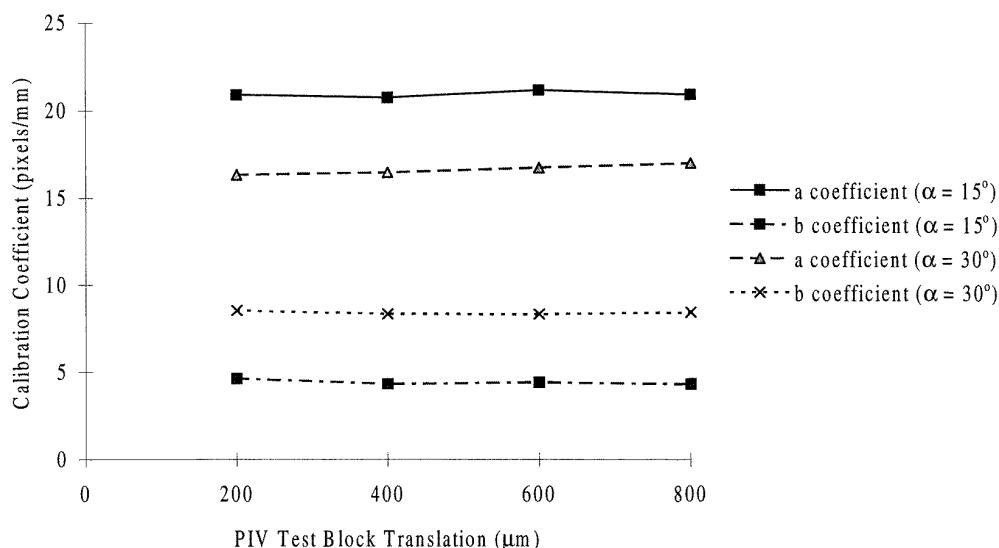


Figure 5. Graph to show linearity of system for a range of PIV test block translations and camera angles ($x/d_0 = 0.1$).

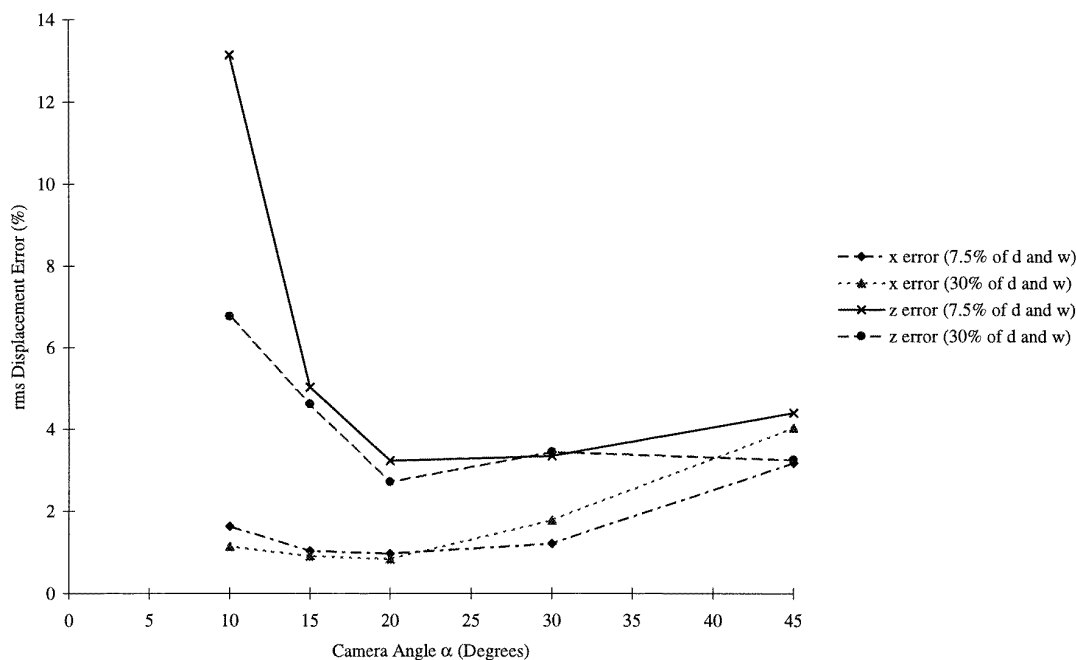


Figure 6. Graph to show PIV system performance in terms of x and z rms errors.

a lower f number hence giving a light power advantage. If, however, sufficient laser power is available and the spatial resolution of the flow structures matches the resolution provided by the CCD, these results have shown a relatively cheap 3D PIV system with high measurement performance is possible by using *in situ* calibration in conjunction with simple processing algorithms.

Previous algorithms developed for particle tracking velocity (PTV) have suggested an optimum camera angle of $\alpha = 45^\circ$ [28] which matches the theoretical error ratio analysis [23] but contradicts the optimum result here

of $20^\circ < \alpha < 30^\circ$. The previous analysis [28], however, used computer generated images which did not include the aberrations generated in this case by camera geometry and by imaging through the PIV test blocks. These optical effects would therefore account for the differences in optimum camera angle of $\alpha = 45^\circ$ [28] and $20^\circ < \alpha < 30^\circ$. Hence the optimum set-up in this stereo system should apply to similar CCD imaging systems. It must be noted though that the test block width for these experiments was limited to 20 mm. This was due to the properties of the resin which contained impurities

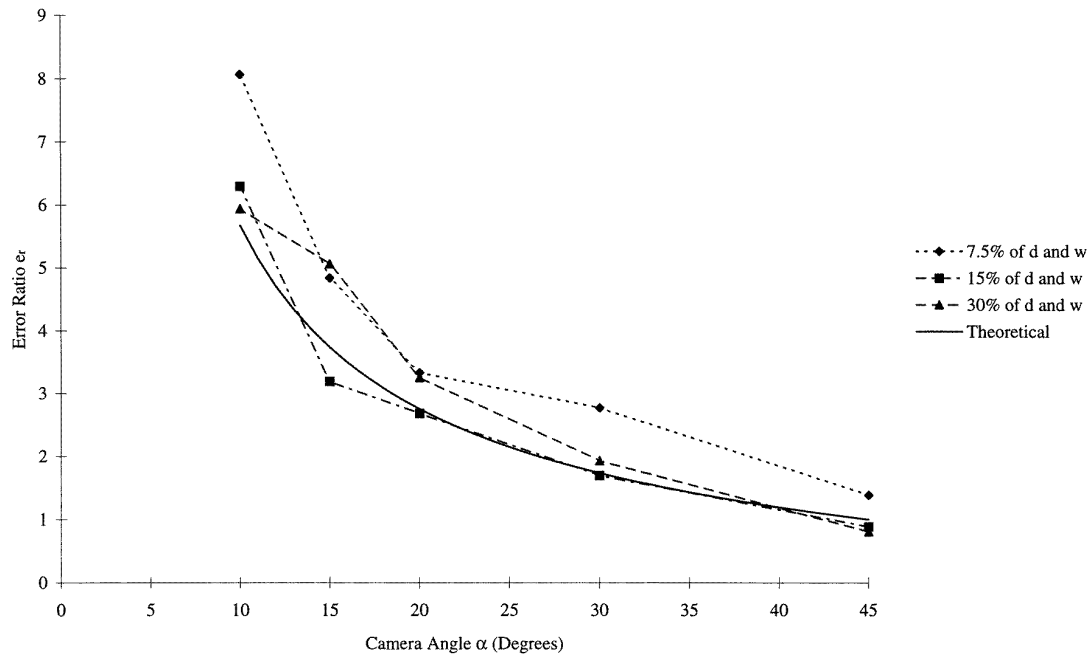


Figure 7. Graph to show experimental and theoretical error ratios for a range of camera angles and particle displacements.

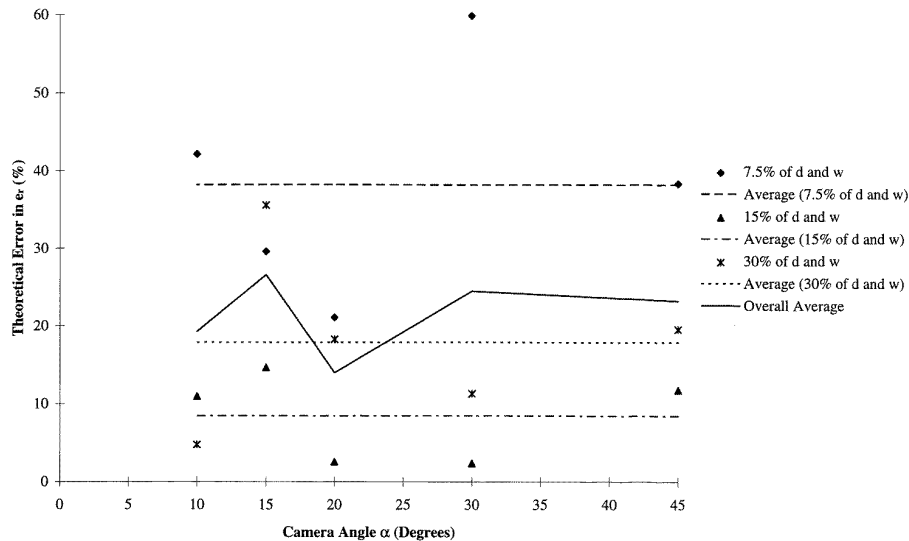


Figure 8. Graph to show the deviations in the theoretical prediction of error ratio.

reducing its visibility and due to moulding imperfections which formed during the gelling stage. Therefore it must be assumed that a thicker block would degrade the image quality further as found in previous work, when using a thick liquid layer [12]. In this situation in order to retain system performance a simple solution is to increase the f number of the imaging system [12, 13]. Further tests were carried to study these effects by placing a PIV test block in the centre of a 600 mm wide water tank and acquiring images using the same object distance. It was

found an additional f number was necessary to achieve the same image quality from simple visual inspection during acquisition. Consequently, higher laser power would be required when taking measurements in wider liquid flows. These tests though did also demonstrate the flexibility of the PIV test block design which can be customized to the rig being measured and be used to calibrate *in situ*.

Previous work discussed in detail the problems of image registration and calibration in stereo PIV systems [23]. With photographic systems, moiré techniques and

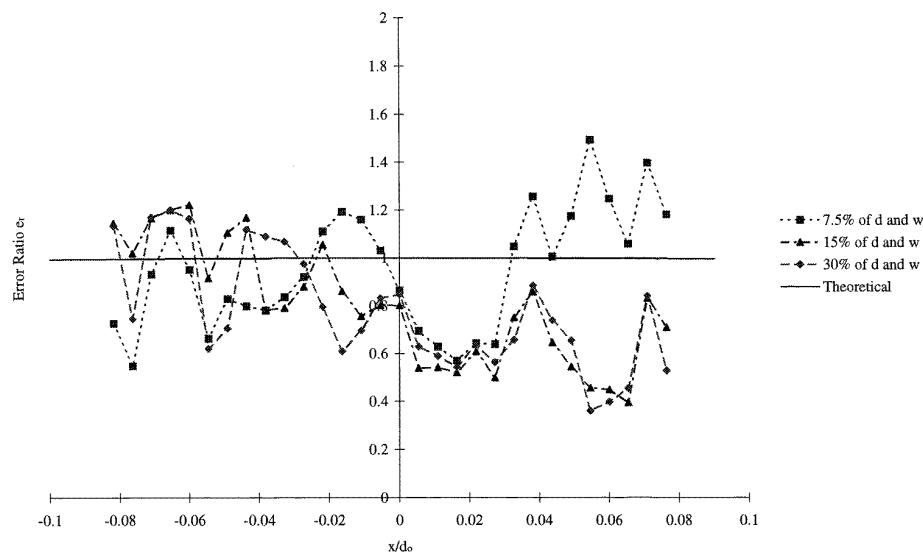


Figure 9. Graph to show the variation of error ratio across the image plane ($\alpha = 45^\circ$).

double imaging onto a single transparency have been used to overcome the registration uncertainty [12,13]. In this system, however, the use of bicubic spline interpolations was relied upon throughout the image processing stage to ensure point to point correspondence of any ΔX displacements and calibration coefficients. For the simple uniform flow test images used in this study, these techniques obviously provided acceptable accuracy. If considerably more complex flow regimes are to be measured, however, careful choice of the interpolation grid resolution would be required to maintain the accuracy of the interpolation functions. This issue was not investigated in this study and further work is required in this area.

5. Conclusions

This paper has demonstrated and tested a simple design of digital angular stereoscopic PIV system. Results from the tests have shown optimum performance will be obtained by using camera angles of between 20 and 30° and camera f numbers of $f16$ and higher. With this set-up and if measuring a uniform flow then in plane and out of plane rms errors will be 1–2 and 3–4% respectively. The results have also shown a theoretical prediction of system performance derived in previous work [23] which considers the ratio of out of plane to in plane errors matches to within 8 and 18% of the experimental system performance providing particle displacements are restricted between 15 and 30% of the interrogation region length. Error ratios in this case were around two. Below this displacement range, the random errors in measurement caused unacceptable deviation from the theoretical predictions and an increase in imaging resolution was suggested to reduce this problem.

References

- [1] Ower E and Pankhurst R C 1966 *The Measurement of Air Flow* 4th edn (New York: Pergamon) pp 6–24
- [2] Durst F, Melling A and Whitelaw J H 1981 *Principles and Practice of Laser Doppler Anemometry* (New York: Academic)
- [3] Adrian R J 1991 Particle-imaging techniques for experimental fluid mechanics *Annu. Rev. Fluid Mech.* **23** 261–304
- [4] Pickering C J D and Halliwell N A 1985 Particle image velocimetry: a new field measurement technique *Optical Measurement in Fluid Dynamics (Inst. Phys. Conf. Ser. 77)* session 4 (Bristol: Hilger)
- [5] Mao Z Q, Halliwell N A and Coupland J M 1993 Particle image velocimetry: high-speed transparency scanning and correlation-peak location in optical processing systems *Appl. Opt.* **32** 5089–91
- [6] Meinhardt C D, Prasad A K and Adrian R J 1993 A parallel digital processor system for particle image velocimetry *Meas. Sci. Technol.* **4** 619–26
- [7] Reeves M, Garner C P, Dent J C and Halliwell N A 1994 Particle image velocimetry measurements of barrel swirl in a production geometry optical IC engine *SAE Paper* 940241
- [8] Stolz W, Kohler J, Lawrenz W, Meier F, Bloss W H, Maly R R, Herweg R and Zahn M 1992 Cycle resolved flow field measurements using a PIV movie technique in a SI engine *SAE Paper* 922354
- [9] Hinsch K D 1995 Three-dimensional particle velocimetry *Meas. Sci. Technol.* **6** 742–53
- [10] Coupland J M and Halliwell N A 1992 Particle image velocimetry: three-dimensional fluid velocity measurements using holographic recording and optical correlation *Appl. Opt.* **31** 1005–7
- [11] Barnhart D H, Adrian R J and Papen G C 1994 Phase-conjugate holographic system for high resolution particle image velocimetry *Appl. Opt.* **33** 7159–70
- [12] Prasad A K and Adrian R J 1993 Stereoscopic particle image velocimetry applied to liquid flows *Exp. Fluids* **15** 49–60
- [13] Arroyo M P and Greated C A 1991 Stereoscopic particle image velocimetry *Meas. Sci. Technol.* **2** 1181–6
- [14] Grant I, Zhao Y, Tan Y and Stewart J N 1991 Three component flow mapping: experiences in stereoscopic PIV and holographic velocimetry *Laser Anemometry Advances and Applications* vol 1, ed A Dybbs and B Ghorashi (New York: ASME) pp 365–71

- [15] Westerweel J and Nieuwstadt F T M 1991 Performance tests on 3D velocity measurements with a two-camera digital particle image velocimeter *Laser Anemometry Advances and Applications* vol 1, ed A Dybbs and B Ghorashi (New York: ASME) pp 349–55
- [16] Prasad A K and Jensen K 1995 Scheimpflug stereocamera for particle image velocimetry in liquid flows *Appl. Opt.* **34** 7092–9
- [17] Raffel M, Gharib M, Ronneberger O and Kompenhans J 1995 Feasibility study of three-dimensional PIV by correlating images of particles within parallel light sheets *Exp. Fluids* **19** 69–77
- [18] Brucher C 1996 3D PIV via spatial correlation in a color-coded light sheet *Exp. Fluids* **21** 312–4
- [19] Grant I, Fu S, Pan X and Wang X 1995 The application of an in-line, stereoscopic, PIV system to 3-component velocity measurements *Exp. Fluids* **21** 214–21
- [20] Keane R D and Adrian R J 1990 Optimisation of particle image velocimeters. Part I: double pulsed systems *Meas. Sci. Technol.* **1** 1202–15
- [21] Prasad A K, Adrian R J, Landreth C C and Offutt P W 1992 Effect of resolution on the speed and accuracy of particle image velocimetry interrogation *Exp. Fluids* **13** 105–16
- [22] Keane R D and Adrian R J 1992 Theory of cross correlation analysis of PIV images *J. Appl. Sci. Res.* **49** 191–215
- [23] Lawson N J and Wu J 1997 Three-dimensional particle image velocimetry: error analysis of stereoscopic techniques *Meas. Sci. Technol.* **8** 894–900
- [24] Press W H, Teukolsky S A, Vetterling W T and Flannery B P 1992 *Numerical Recipes in Fortran—The Art of Scientific Computing* 2nd edn (New York: Cambridge University Press)
- [25] Goodman W G 1968 *Introduction to Fourier Optics* (New York: McGraw-Hill) pp 275–80
- [26] Westerweel J 1993 Analysis of PIV interrogation with low pixel resolution *Optical Diagnosis in Fluid and Thermal Flow (San Diego, 1993)*, *SPIE* vol 2005, ed S S Cha and J D Trolinger (Bellingham, WA: SPIE) pp 624–35
- [27] Landreth C C and Adrian R J 1988 Measurement and refinement of velocity data using high image density analysis in particle image velocimetry *Proc. 4th Int. Symp. on the Applications of Laser Anemometry to Fluid Mechanics (Lisbon, 1988)* ed R J Adrian *et al*, pp 491–7
- [28] Guezennec Y G, Brodkey R S, Trigui N and Kent J C 1994 Algorithms for fully automated three-dimensional particle tracking velocimetry *Exp. Fluids* **17** 209–19